J. Fluid Mech. (2018), *vol.* 844, *pp.* 956–969. © Cambridge University Press 2018
doi:10.1017/jfm.2018.218

Intrusions propagating into linearly stratified ambients

M. A. Khodkar[1], K. El Allam[1,2] and E. Meiburg[1,†]

[1]Department of Mechanical Engineering, University of California at Santa Barbara, Santa Barbara, CA 93106, USA

[2]Graduate School of Engineering, ENSEIRB-MATMECA, 33400 Talence, France

(Received 9 August 2017; revised 28 February 2018; accepted 6 March 2018; first published online 13 April 2018)

Equilibrium and non-equilibrium intrusions released from long, full-depth locks and advancing into linearly stratified ambients are investigated via a vorticity-based modelling approach, for the constant-velocity slumping phase. Non-equilibrium intrusions give rise to an upstream-propagating wave, which we model as a bore. Predictions by the vorticity model agree closely with two-dimensional direct numerical simulation results and earlier experimental and computational data regarding front velocities, current thicknesses as well as the height and propagation velocity of the bore.

Key words: geophysical and geological flows, gravity currents, stratified flows

1. Introduction

An intrusive gravity current, or intrusion, forms when a fluid of one density propagates laterally into a stratified ambient along an intermediate height. While several earlier studies addressed the case of two-layer stratified ambients (e.g. Holyer & Huppert 1980; de Rooij, Linden & Dalziel 1999; Lowe, Linden & Rottman 2002; Sutherland, Kyba & Flynn 2004; Cheong, Kuenen & Linden 2006; Flynn & Linden 2006; Khodkar, Nasr-Azadani & Meiburg 2016), the current investigation focuses on intrusions propagating into linearly stratified ambients. Such flows can be generated in the laboratory via a lock-release experiment, as sketched in figure 1. The left half of a rectangular tank of length L and height H is initially filled with fluid of intermediate density ρ_c, while the right half contains a stratified fluid whose density varies linearly from ρ_u at the top to ρ_l at the bottom. Upon releasing the flow, the fluid of density ρ_c forms a right-propagating intrusion that travels with velocity U_c. Concurrently, the ambient fluid forms two counterflowing gravity currents along the lower and upper walls that propagate with U_l and U_u, respectively. Earlier studies (Bolster, Hang & Linden 2008; Munroe *et al.* 2009; Maurer, Bolster & Linden 2010) demonstrate that the flow is symmetric with respect to the midplane of the tank when $\rho_c = (\rho_l + \rho_u)/2$. Under these conditions, the neutral buoyancy isopycnal ahead of the intrusion remains flat, as shown in figure 1(*a*). On the other hand, when the intrusion density differs from the average ambient density, a non-symmetric intrusion forms as

†Email address for correspondence: meiburg@engineering.ucsb.edu

https://doi.org/10.1017/jfm.2018.218 Published online by Cambridge University Press

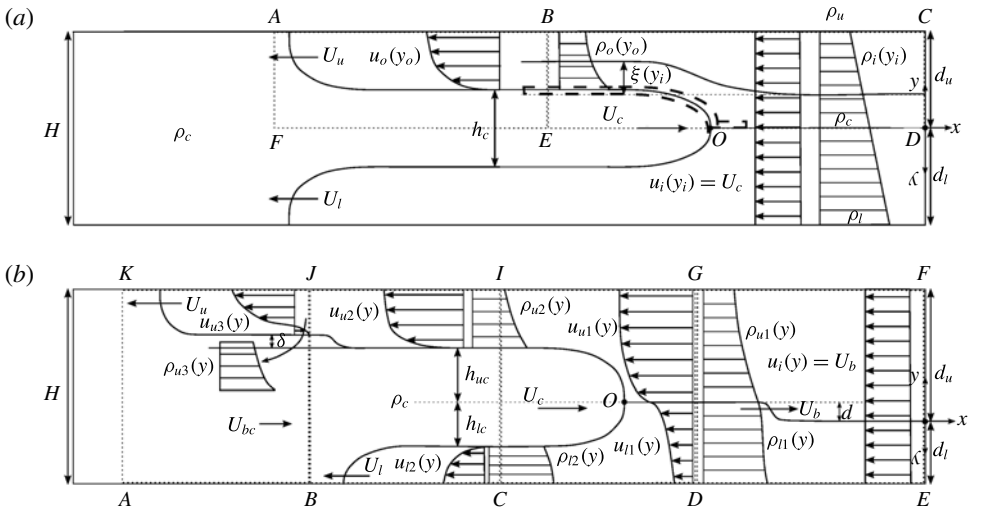


FIGURE 1. Lock-release flow of an intrusion into a linearly stratified ambient: (*a*) symmetric case; (*b*) non-symmetric case. For the symmetric case, the interface ahead of the intrusion remains unperturbed, whereas an upstream-propagating bore forms for the non-symmetric case. For the latter, the left-propagating gravity currents travel with different velocities, and the faster current gives rise to a bore at the same streamwise location as the front of the slower current. The dotted lines indicate the various control volumes for which mass and vorticity balances are established.

sketched in figure 1(*b*). Here the countercurrents along the top and bottom walls have different velocities, and the flow generates an upstream-propagating wave that travels ahead of the intrusion. Munroe *et al.* (2009) and Maurer & Linden (2014) observe that the wave amplitude varies across the tank height, and that this amplitude has a maximum near the neutral buoyancy isopycnal. A left-propagating bore also forms along the interface between the faster counterflowing current and the intrusion, at the streamwise location of the front of the slower counterflowing current. The degree of asymmetry in the flow can conveniently be expressed by the quantity

$$\epsilon = \left| \frac{\rho_c - 0.5(\rho_u + \rho_l)}{\rho_l - \rho_u} \right|. \tag{1.1}$$

Efforts to develop analytical models for flows with arbitrary stratification date back over half a century. Based on the streamfunction–vorticity formulation for two-dimensional, incompressible, inviscid flows, Long (1953) obtained a partial differential equation for the displacement of streamlines. Less general forms of this equation were later employed by Ungarish (2006) and White & Helfrich (2008) to study gravity currents travelling into linearly stratified ambients. The ordinary differential equation (ODE) derived by Nasr-Azadani & Meiburg (2016) for gravity currents advancing into linear stratification corresponds to the equation of Long (1953), if derivatives are taken with respect to the upstream vertical coordinates of the streamlines.

The first analytical model for symmetric intrusions propagating into linearly stratified ambients was proposed by Ungarish (2005), based on a shallow-water approach. A similar model was also developed for bottom-propagating gravity currents in linear stratification by Ungarish & Huppert (2002), while Ungarish & Huppert

https://doi.org/10.1017/jfm.2018.218 Published online by Cambridge University Press

(2006) compare the energy budget of the flow given by this one-layer shallow-water model with that provided by numerical simulations. This model considers intrusions during both the constant-velocity (slumping) and the time-dependent-velocity (self-similar) phases, and it investigates intrusions released from partial- as well as full-depth locks, cf. also Ungarish (2009).

Bolster *et al.* (2008) develop a model for intrusions propagating into linearly stratified ambients by extending the approach of Cheong *et al.* (2006). They obtain for the intrusion velocity

$$\frac{U_c}{\hat{g}H} = \frac{F}{2}\sqrt{12\epsilon^2 + 1}. \tag{1.2}$$

Depending on whether they calibrate with the results of Maxworthy *et al.* (2002) or Ungarish (2006), they obtain F-values of 0.266 or 0.25, respectively. Here $\hat{g}$ denotes the reduced gravity $g(\rho_l - \rho_u)/\rho_c$. Bolster *et al.* (2008) observe that the intrusion head becomes subcritical with respect to internal waves of mode-1 as soon as the symmetry condition is broken, and also with respect to internal waves of mode-2 as long as $\epsilon < 0.23$. They do not incorporate the wave energy into their model, based on the assumption that this energy component is much smaller than the potential and kinetic energies associated with the mean flow. An attempt to evaluate the contribution of the wave energy to the overall budget was made by Munroe *et al.* (2009) and Maurer & Linden (2014).

Within the current study, we extend the vorticity-based modelling concept to intrusive gravity currents propagating into linearly stratified ambients. This approach was first introduced by Borden & Meiburg (2013*a*) and Borden & Meiburg (2013*b*) for gravity currents and bores, and subsequently extended by Nasr-Azadani & Meiburg (2016) to flows with continuous stratification. It relies on the principles of mass and vorticity conservation only, and avoids the need for energy-related arguments. Based on the experimental observations of Munroe *et al.* (2009), who showed that intrusions in linearly stratified ambients can propagate at constant speeds from 5 up to 20 times of the lock length (depending on whether the intrusion is symmetric or non-symmetric), we limit ourselves to the slumping phase and to the intrusions generated from a full-depth lock release. In addition, since we intend to focus on the upstream-propagating wave ahead of the intrusion, we take the lock length sufficiently long so that wave reflection from the rear wall will not be important. Section 2 develops vorticity models for both equilibrium and non-equilibrium intrusions. In § 3, we perform direct numerical simulations, whose results are compared in § 4 to the corresponding vorticity model predictions, as well as to theoretical and experimental findings of other authors. Section 5 presents a brief summary.

2. Theory

2.1. *Symmetric intrusions*

Due to their symmetry properties with respect to the channel centreline, symmetric intrusions can be analysed based on the upper half of the domain only, cf. figure 1(*a*). Hence, we are effectively dealing with a bottom gravity current propagating into a linearly stratified ambient in a domain of height $H/2$. Nasr-Azadani & Meiburg (2016) analyse such flows under the assumption of inviscid vorticity dynamics in the Boussinesq limit, in the reference frame moving with the gravity current. We remark this assumption of inviscid vorticity dynamics does not necessarily imply that the flow is energy conserving. Nasr-Azadani & Meiburg (2016) show that the conservation of mass and vorticity result in a second-order ODE for the vertical displacement ξ of

https://doi.org/10.1017/jfm.2018.218 Published online by Cambridge University Press

a streamline between the upstream and downstream boundaries, as a function of its vertical inflow location y_i

$$\xi'' u_i^2 + \xi'(1+\xi')(2+\xi')u_i u_i' - \xi(1+\xi')^3 g\frac{\rho_i'}{\rho_c} = 0. \tag{2.1}$$

Here $\rho_i(y_i)$ and $u_i(y_i)$ denote the density and horizontal velocity distributions at the inflow boundary, respectively. y_i varies from 0 to $H/2$, where $y_i = 0$ is located at the neutral buoyancy isopycnal y_N

$$y_N = \left(1 - \frac{\rho_c - \rho_u}{\rho_l - \rho_u}\right) H, \tag{2.2}$$

which is identical to the channel centreline for symmetric intrusions. Substituting the upstream flow conditions corresponding to figure 1(*a*) into (2.1) results in

$$\xi'' U_c^2 + \xi(1+\xi')^3 g N^2 = 0, \tag{2.3}$$

with buoyancy frequency N equal to $\sqrt{g(\rho_l - \rho_u)/(\rho_c H)}$. As boundary conditions we have $\xi(H/2) = 0$ and $\xi(0) = h_c/2$, where the intrusion height h_c is unknown. Vorticity conservation along the upper interface of the intrusion gives

$$\frac{u_o(0)^2}{2} = g\frac{\rho_i(0) - \rho_c}{\rho_c}\frac{h_c}{2} = 0, \tag{2.4}$$

where u_o indicates the horizontal velocity at the outflow boundary of control volume *EDCB*. This equation is obtained by applying the vorticity conservation principle to the infinitesimal control volume whose top and bottom boundaries are immediately above and below the upper interface of the intrusion (dashed lines in figure 1*a*). Clearly there is no influx of vorticity into this control volume, since the upstream velocity is uniform. Furthermore, as the width of this control volume decreases, the density difference across the outflow boundary of the control volume decreases as well, and it tends to zero in the limit of a vanishingly thin control volume, so that no vortex sheet forms along the interface. Hence, at the interface the ambient has the same velocity as the intrusion, so that $u_o(0) = 0$ in the reference frame moving with the intrusion. By applying the conservation of mass to an infinitesimal streamtube, Nasr-Azadani & Meiburg (2016) show

$$u_o(y_i) = \frac{u_i(y_i)}{1+\xi'}, \tag{2.5}$$

so that we obtain $\xi'(0) = \infty$. This boundary condition is different from those of Ungarish (2006) and White & Helfrich (2008) for boundary-propagating gravity currents, since both of those studies obtain their closure equation from using Bernoulli's equation. An additional equation for the unknown intrusion thickness h_c can be obtained by applying the inviscid integral vorticity conservation equation

$$\oint \omega \boldsymbol{u}\cdot\boldsymbol{n}\,\mathrm{d}S = -\iint \frac{g}{\rho_c}\frac{\partial\rho}{\partial x}\,\mathrm{d}A, \tag{2.6}$$

to control volume *FEBA* in the reference frame moving leftward with the velocity U_u of the upper gravity current. Here ω and $\boldsymbol{u}$ represent the vorticity normal to the

https://doi.org/10.1017/jfm.2018.218 Published online by Cambridge University Press

plane and the velocity vector, respectively. dA, dS and $\boldsymbol{n}$ indicate a differential area within the control volume, a differential length along the boundaries of the control volume and the unit outer normal vector to the control volume boundaries. For *FEBA*, equation (2.6) reduces to

$$\frac{1}{2}\Big\{(U_u+U_c)^2-\big[U_u-\big(u_o(H/2)-U_c\big)\big]^2\Big\}=\int_{h_c/2}^{H/2}\frac{g}{\rho_c}\big[\rho_c-\rho_o(y)\big]\,\mathrm{d}y. \tag{2.7}$$

We evaluate U_u as the average horizontal velocity within the upper gravity current in the laboratory frame

$$U_u=\frac{\displaystyle\int_{h_c/2}^{H/2}\big[u_o(y)-U_c\big]\,\mathrm{d}y}{H/2-h_c/2}. \tag{2.8}$$

Here $U_u-[u_o(H/2)-U_c]$ is the horizontal velocity along the top wall at B, in the reference frame moving with the upper gravity current.

We can then solve the vorticity model equations as follows: after guessing initial values for h_c and U_c, we integrate equation (2.3) subject to the boundary conditions $\xi(0)=h_c/2$ and $\xi'(0)=\infty$. The latter is implemented by setting $\xi'(0)$ to a large number. Tests show that for sufficiently large values $\xi'(0)>10^3$, the numerical solution does not depend on the exact value chosen. Then we perform an inner iteration loop by updating our guess for h_c via a bisection shooting procedure until the condition $|\xi(H/2)|<10^{-7}$ is satisfied. The final value for U_c is then found via an outer iteration loop, as follows: since the density remains constant along a streamline, we can evaluate the outflow density $\rho_o(y)$ from $\rho_o(y_i+\xi(y_i))=\rho_i(y_i)$, and the outflow velocity $u_o(y)$ is obtained from (2.5). We then iterate on U_c until (2.7) is satisfied within the control volume *FEBA* with an error less than 10^{-7}.

2.2. *Non-symmetric intrusions*

If the symmetry condition is violated, a non-equilibrium intrusion such as the one sketched in figure 1(*b*) forms, giving rise to an upstream-propagating wave. This wave travels with uniform velocity for all isopycnals (Munroe *et al.* 2009; Maurer & Linden 2014)). Its amplitude vanishes at the top and bottom walls and has a maximum close to the neutral buoyancy isopycnal, as discussed earlier. In the following, we treat this leading wave as a bore that has an amplitude d at the neutral buoyancy isopycnal and travels with velocity U_b. The validity of this assumption will be further examined in § 4. To solve for the speed and the amplitude of this bore, we employ a vorticity-based analysis similar to that of § 2.1, by applying (2.1) separately to the upper and lower regions of control volume *DEFG*, in the reference frame moving with the bore. We thus obtain

$$\xi''U_b^2+\xi(1+\xi')^3N^2=0. \tag{2.9}$$

The y-axis is directed upward in the upper region, and downward in the lower region, so that the form of (2.9) remains identical in both regions. As boundary conditions at the interface and the upper and lower walls we have

$$\xi_{u1}(0)=-\xi_{l1}(0)=d, \tag{2.10}$$

$$\xi_{u1}(d_u)=\xi_{l1}(d_l)=0. \tag{2.11}$$

https://doi.org/10.1017/jfm.2018.218 Published online by Cambridge University Press

Furthermore, the solution has to be smooth at the interface, so that

$$\xi'_{u1}(0) = \xi'_{l1}(0). \tag{2.12}$$

We then set up an iterative solution procedure, with an inner loop for U_b and an outer one for d, along the following lines: based on initial guesses for these two variables we solve (2.9) for the upper and lower regions based on boundary conditions (2.10) and (2.11), via a bisection shooting method. In this way we obtain the slopes of the deflection at the neutral buoyancy isopycnal $\xi'_{u1}(0)$ and $\xi'_{l1}(0)$. We then iterate on U_b until (2.12) holds. We verify the validity of the d-value later, and iterate on that, if needed.

The above provides us with preliminary density and velocity distributions upstream of the intrusion. Due to the propagation of internal gravity waves upstream of the intrusion, the density stratification ahead of the intrusion will no longer be linear and the velocity distribution exhibits shear, so that the more general equation (2.1) has to be employed to obtain the intrusion speed and thickness. Towards this end, we first investigate the flow within the slower left-propagating current, which is the lower one when $\rho_c > (\rho_l + \rho_u)/2$. Next, we guess a value for U_c and shift the reference frame from the leading bore to the intrusion by replacing u_i with $u_{l1} - U_b + U_c$ in (2.1). We then find the thicknesses of the lower gravity current and lower branch of the intrusion, h_l and h_{lc}, as well as the intrusion speed U_c by using the same numerical procedure as that described for a symmetric intrusion, except that the closure equation should be modified as we apply the vorticity conservation equation (2.6) to the region below the stagnation point of the intrusion (O in figure 1*b*) and inside control volume *BCIJ*, while travelling with the bottom-propagating current, which leads to

$$\frac{1}{2}\left\{(U_l + U_c)^2 - \left[U_l - (u_{l2}(d_l + d) - U_c)\right]^2\right\} = \int_{h_{lc}}^{d_l+d} \frac{g}{\rho_c}(\rho_{l2}(y) - \rho_c)\,\mathrm{d}y. \tag{2.13}$$

U_l in the above equation can be calculated in the same fashion as U_u in § 2.1

$$U_l = \frac{\displaystyle\int_{h_{lc}}^{d_l+d} \left[u_{l2}(y) - U_c\right]\mathrm{d}y}{h_l}. \tag{2.14}$$

Computing U_c enables us to solve for the flow properties within the upper branch of the intrusion, when we substitute u_i and ρ_i with $u_{u1} - U_b + U_c$ and ρ_{u1}. We then guess a value for h_{uc} and correct our guess until integrating from ODE (2.1) yields $|\xi_{u2}(d_u - d)| < 10^{-7}$. The thickness h_c of the intrusion can then be computed as $h_{lc} + h_{uc}$.

Evaluation of the flow variables downstream of the intrusion then allows us to determine the properties of the left-propagating internal bore, which travels at the same speed as the slower counterflowing current (here U_l). Thus, we only need to find its amplitude to obtain the flow condition downstream of the bore. Towards this end, we make a guess for the amplitude δ and solve (2.1) in an iterative fashion, with slope $\xi'_{u3}(0)$ equal to

$$\xi'_{u3}(0) = \frac{U_c + U_l}{U_{bc} + U_l} - 1. \tag{2.15}$$

https://doi.org/10.1017/jfm.2018.218 Published online by Cambridge University Press

This condition is obtained using (2.5) along the interface of the bore. U_{bc} can also be calculated by employing the continuity equation within the intrusion fluid and in the reference frame moving with the left-propagating bore

$$(U_{bc} + U_l)(H - h_u) = (U_c + U_l)h_c. \tag{2.16}$$

This ODE has to be solved concurrently along with (2.15) and (2.16) to obtain the bore amplitude δ in addition to the flow properties downstream of the bore.

The above analysis evaluates the properties of all flow components for the preliminary d-value. The validity of this d-value can then be checked by examining the vorticity balance within the entire control volume $ABJK$, in the reference frame moving with the top-propagating current. This yields

$$\frac{1}{2}\left\{(U_u + U_{bc})^2 - \left[U_u - (u_{u3}(H) + U_l)\right]^2\right\} = \int_{H-h_u}^{H} \frac{g}{\rho_c}\left[\rho_c - \rho_{u3}(y)\right] \mathrm{d}y, \tag{2.17}$$

where $h_u = H - h_c - h_l - \delta$. If (2.17) holds to within 10^{-7}, we accept the preliminary d-value, otherwise we iterate to obtain an updated value for d.

3. Direct numerical simulation results

To assess the predictive capabilities of the vorticity model, we perform two-dimensional direct numerical simulations with our in-house software TURBINS (Nasr-Azadani & Meiburg 2011; Nasr-Azadani, Hall & Meiburg 2013). Based on a finite-difference approach that utilizes a fractional projection method along with total variation diminishing third-order Runge–Kutta (TVD-RK3) time integration, TURBINS solves the dimensionless Navier–Stokes and density equations in the Boussinesq limit

$$\boldsymbol{\nabla} \cdot \boldsymbol{u}^* = 0, \tag{3.1}$$

$$\frac{\partial \boldsymbol{u}^*}{\partial t^*} + \boldsymbol{u}^* \cdot \boldsymbol{\nabla} \boldsymbol{u}^* = -\boldsymbol{\nabla} p^* + \frac{1}{Re}\nabla^2 \boldsymbol{u}^* + \rho^* \boldsymbol{e}^g, \tag{3.2}$$

$$\frac{\partial \rho^*}{\partial t^*} + \boldsymbol{u}^* \cdot \boldsymbol{\nabla} \rho^* = \frac{1}{Pe}\nabla^2 \rho^*. \tag{3.3}$$

Here, $\boldsymbol{e}^g$ denotes the unit vector in the direction of gravity. The Reynolds and Péclet numbers are defined as $Re = \sqrt{\hat{g}H}H/\nu$ and $Pe = \sqrt{\hat{g}H}H/D$, where H, ν and D represent the channel height, kinematic viscosity and diffusivity of the density field. For the purpose of non-dimensionalization, the reference length, velocity and pressure are taken as H, $\sqrt{\hat{g}H}$ and $\rho_c \hat{g} H$, respectively. The dimensionless density is defined as $\rho^* = (\rho - \rho_u)/(\rho_l - \rho_u)$.

We employ free-slip conditions at all boundaries, along with vanishing normal flux conditions for the density field. Initially, the fluid is at rest everywhere. The left half of the container is filled with the intrusion fluid of constant density ρ_c^*, while the stratified ambient fluid in the right half of the container has an initial density profile $\rho^* = 1 - y^*$. The simulations are carried out for $Re = 3 \times 10^4$ and $Pe = 7.5 \times 10^4$, so that diffusive effects can be assumed small. The computational domain has dimensions $L = 70$ and $H = 1$, and we employ a uniformly spaced grid with $\Delta x^* = 0.01$ and $\Delta y^* = 0.005$.

For a representative symmetric intrusion, figure 2(*a*) shows the density field at $t^* = 60$, along with streamlines in the reference frame moving with the intrusion.

https://doi.org/10.1017/jfm.2018.218 Published online by Cambridge University Press

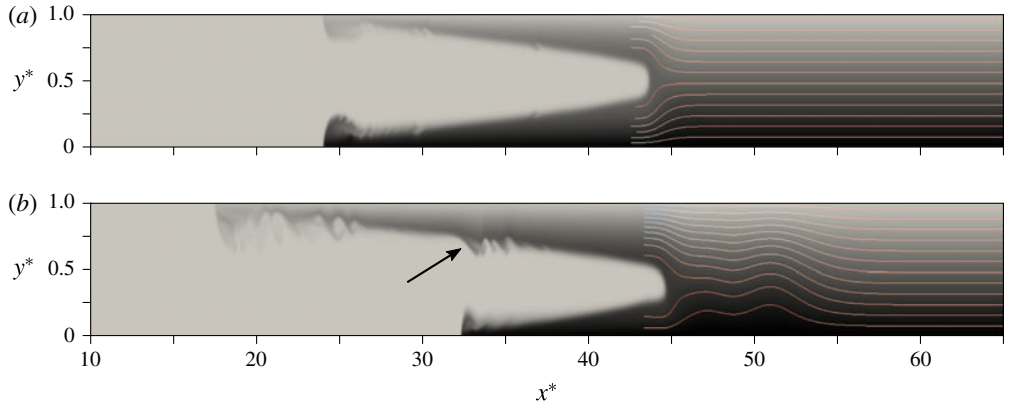


FIGURE 2. Density fields at time $t^* = 60$ for (a) a symmetric intrusion, and (b) a non-symmetric intrusion with $\rho_c^* = 0.7$. The arrow in panel (b) indicates the location of the left-propagating bore. Streamlines upstream of the intrusion are shown in the reference frame moving with the intrusion. Inside the ambient, the density field varies from $\rho^* = 0$ (light grey) to $\rho^* = 1$ (black). The intrusion fluid is shown in light grey, in order to help distinguish it from the ambient fluid.

The neutral buoyancy isopycnal remains undisturbed ahead of the intrusion front, consistent with the assumption of the model developed in § 2.1 for symmetric intrusions ($\rho_c^* = 0.5$). On the other hand, the non-symmetric counterpart in figure 2(b) clearly indicates the presence of a wavefront that propagates faster than the intrusion itself. By conducting simulations for different values of ϵ, we found that for $\epsilon \lesssim 0.2$ the flow typically gives rise to both mode-1 and mode-2 internal waves, with the mode-1 waves travelling nearly twice as fast as the mode-2 waves. For $\epsilon \gtrsim 0.2$, the simulations showed mode-1 waves only. This observation is consistent with earlier findings by Munroe *et al.* (2009) and Maurer & Linden (2014). We remark that these waves are more directly comparable to those observed by Maurer & Linden (2014), rather than to the waves reflected from the rear wall identified by Munroe *et al.* (2009). In contrast to earlier studies, we note that the waviness of the isopycnals in figure 2(b) exhibits two distinguishable peaks, which can be attributed to the longer locks employed here. In addition, the simulations showed that the deflections of all isopycnals travel at the same speed, and that the maximum deflection always occurs close to the neutral buoyancy isopycnal, which allows us to treat the leading wave as a hydraulic bore.

In order to track the intrusion and ambient fluids, we mark them with different passive 'computational dyes' that have the same diffusivity as the density field. If we denote the dimensionless dye concentration by c_d^*, we can define the local height η^* of the right-propagating intrusions or the left-propagating gravity currents as

$$\eta^*(x^*, t^*) = \int_0^1 c_d^*(x^*, y^*, t^*)\, \mathrm{d}y^*. \tag{3.4}$$

The front location x_f^* of a current is then obtained as the first point with $\eta^* > 0.01$.

Figure 3(a) depicts the front locations of the upper and lower gravity currents and the intrusion as functions of time, for the non-symmetric intrusion of figure 2(b). After a brief transient period all three fronts are seen to acquire quasisteady velocities, as

https://doi.org/10.1017/jfm.2018.218 Published online by Cambridge University Press

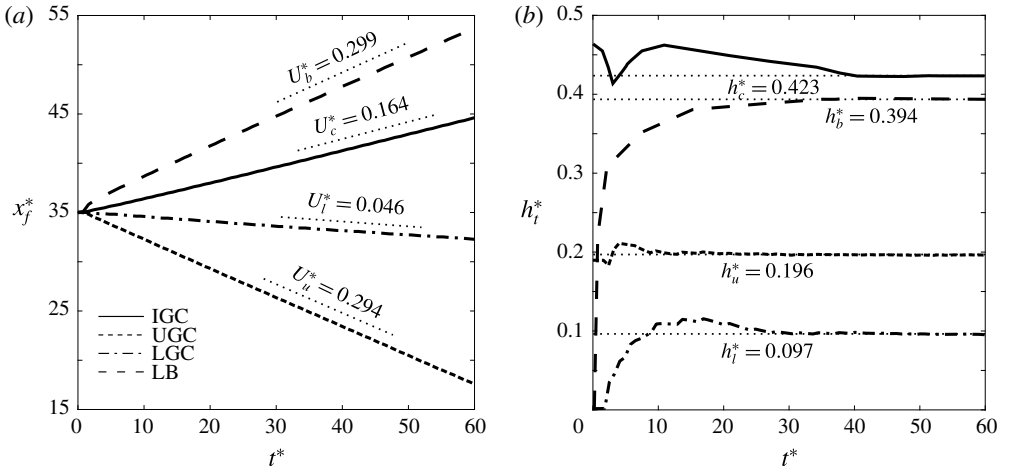


FIGURE 3. (*a*) Front locations, and (*b*) current thicknesses as functions of time, for the direct numerical simulation (DNS) of figure 2(*b*). IGC, UGC and LGC denote the intrusive, upper and lower gravity currents, respectively, while LB refers to the leading bore. The straight line segments in panel (*a*) represent the quasisteady front velocities, obtained by linear fits of the DNS results, while the dotted lines in panel (*b*) indicate the quasisteady heights, evaluated as described in the text.

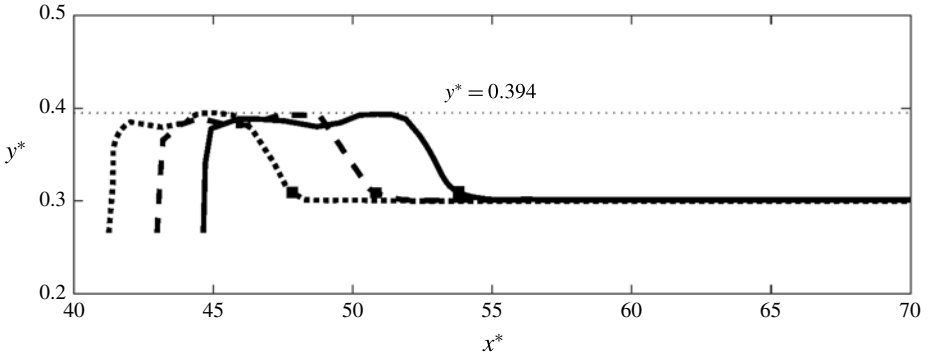


FIGURE 4. Temporal evolution of the neutral buoyancy isopycnal regarding the flow shown in figure 2(*b*), for times $t^* = 40$ (dotted line), 50 (dashed line) and 60 (solid line). The black squares represent the respective front locations of the bore at these times. The horizontal dotted line indicates the quasisteady value of the maximum height h_b^* of the neutral buoyancy isopycnal.

indicated by the dotted straight line segments. We can then define an effective, time-dependent intrusion height $h_{t,c}^*$ by averaging the local intrusion height from the gate location to the intrusion front. The heights $h_{t,l}^*$ and $h_{t,u}^*$ of the lower and upper gravity currents are calculated correspondingly. Figure 3(*b*) indicates that all current heights approach quasisteady values beyond $t^* = 40$, so that we can obtain time-independent current heights h^* by averaging the DNS results from $t^* = 40$ to $t^* = 60$.

Figure 4 represents the shape of the neutral buoyancy isopycnal for the simulation of figure 2(*b*), for three different times in the quasisteady regime. The figure confirms that the front of this isopycnal propagates in a bore-like fashion. We define the

https://doi.org/10.1017/jfm.2018.218 Published online by Cambridge University Press

front location $x^*_{f,b}$ of this bore, indicated by black squares, as the rightmost point along the neutral buoyancy isopycnal where its vertical coordinate is 0.01 above the neutral buoyancy level y^*_N. An effective height h^*_b of the neutral buoyancy isopycnal downstream of the bore is obtained by temporally averaging the instantaneous maximum height $h^*_{t,b}$ of this isopycnal between $t^* = 40$ and $t^* = 60$, as indicated by the horizontal dotted line in figure 4. The bore amplitude d^* is then calculated as $d^* = |h^*_b - y^*_N|$.

For the non-symmetric intrusion of figure 2(*b*), the bore location $x^*_{f,b}$ and its instantaneous maximum height $h^*_{t,b}$ are shown in figure 3 as functions of time. We recognize that for large times both the bore velocity and the bore height achieve quasisteady values. By carrying out a corresponding analysis for other isopycnals, we confirm that all of them propagate with the same velocity. This procedure furthermore yields the displacement magnitude as function of the isopycnal. We find that the largest displacement value d^*_{max} occurs close to the neutral buoyancy level. We refer to d^*_{max} as the maximum wave amplitude, consistent with Munroe *et al.* (2009) and Maurer & Linden (2014).

4. Comparison of model predictions and simulation results

Figure 5 displays the propagation velocity U^*_b and the amplitude d^* of the bore, along with the maximum deflection d^*_{max} of the isopycnals, as functions of ρ^*_c. Shown are DNS results, vorticity model predictions, the estimates of Munroe *et al.* (2009) and the experimental data reported by Maurer & Linden (2014). The vorticity model predicts a constant bore propagation velocity $U^*_b \approx 1/\pi$, which is the theoretical propagation velocity of linear mode-1 waves (McEwan & Baines 1974). Since non-symmetric intrusions always give rise to mode-1 waves, and since these travel faster than any higher-order modes, it is consistent that the leading wave front travels with this velocity. The fact that mode-2 waves are symmetric with respect to the midplane of the tank, so that they result in smaller net displacements of the isopycnals (Bolster *et al.* 2008), further supports this observation. By itself, the vorticity model does not yield any information with regard to the propagation velocity and amplitude of the mode-2 waves. In order to obtain such information, one would have to employ the full ODE to account for the waviness of the isopycnals upstream of the intrusion. The vorticity model predictions regarding U^*_b generally agree with the DNS results to within about 10 %. They are also in reasonable agreement with experimental results of Maurer & Linden (2014). Especially for near-symmetric intrusions, this is somewhat closer than the empirical formula of Munroe *et al.* (2009). For $\epsilon \to 0.5$ (or $\rho^*_c \to 0, 1$), on the other hand, the vorticity model predictions agree closely with this empirical formula. As shown in figure 5(*b*) the vorticity model predicts that $d^* \approx d^*_{max}$ for near-equilibrium intrusions, while they increasingly differ from each other as ϵ grows. Interestingly, for strongly non-symmetric intrusions the vorticity model predictions for d^* are very close to the d^*_{max}-estimates of Munroe *et al.* (2009). The vorticity model predictions for both d^* and d^*_{max} generally agree well with corresponding DNS results, although there is a noticeable discrepancy in regard to the experimental data of Maurer & Linden (2014).

Figure 6 shows model predictions, experimental data and DNS results for the propagation velocities and thicknesses of all three fronts, as functions of ρ^*_c. Figure 6(*a*) demonstrates good agreement among all data sets regarding the intrusion velocity. U^*_c for equilibrium intrusions can furthermore be compared to the result of Ungarish (2005) for an intrusion propagating in a linearly stratified tank, and to the finding of

https://doi.org/10.1017/jfm.2018.218 Published online by Cambridge University Press

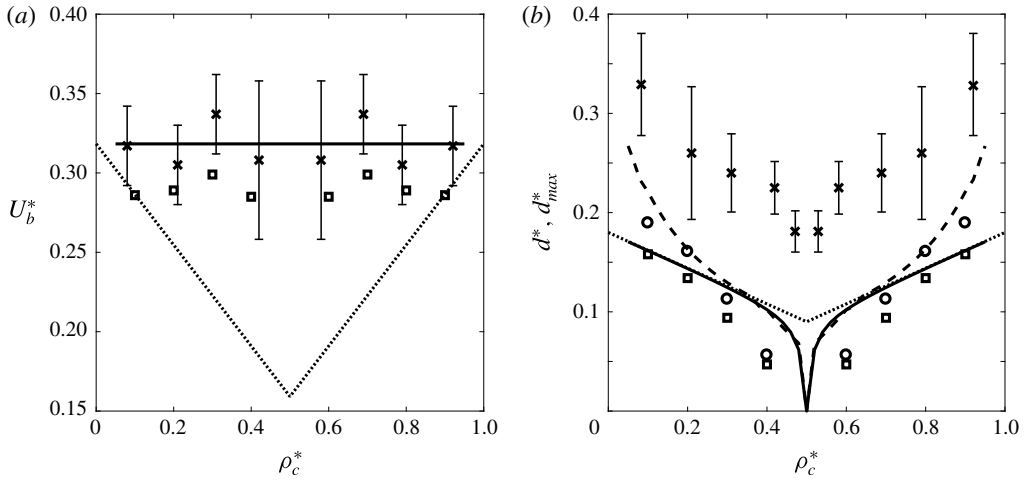


FIGURE 5. (*a*) Propagation speed U_b^* of the bore, and (*b*) maximum displacement d^* of the neutral buoyancy isopycnal as well as the maximum isopycnal deflection d_{max}^*, as functions of the dimensionless intrusion density ρ_c^*. In panel (*a*), the solid line represents the vorticity model prediction, while the dotted line indicates the estimate of Munroe *et al.* (2009). The discrete squares and crosses also denote the DNS results and experimental results of Maurer & Linden (2014). In panel (*b*), the solid and dashed lines represent the vorticity model predictions for d^* and d_{max}^*, respectively, while the dotted line indicates the estimate of Munroe *et al.* (2009) for d_{max}^*. The discrete squares, circles and crosses reflect the DNS results for d^* and d_{max}^* as well as the experimental data reported by Maurer & Linden (2014) for d_{max}^*, respectively.

Ungarish (2006) for a bottom-propagating gravity current whose density is identical to that at the base of the stratification. Both of these results are slightly larger than, but within 5 % of the vorticity model prediction. The small difference between the numerical and experimental results in figure 6(*a*), specifically when $\rho_c^* = 0$ or 1, can be attributed to employing free-slip boundary conditions as well as longer locks in the present DNS in comparison with the experiments of Bolster *et al.* (2008). We also remark that the present simulations are carried out for a two-dimensional configuration, rather than the three-dimensional experimental results of Bolster *et al.* (2008). Both the vorticity model and the DNS data show that for intermediate intrusion densities the intrusion thickness attains a local minimum at $\rho_c^* = 0.5$, as seen in figure 6(*b*). However, in the limits of $\rho_c^* = 0$ and 1 the DNS data indicate an even smaller intrusion thickness than for the symmetric case. In this context, we note that the vorticity model breaks down for $\rho_c^* \to 0$ and $\rho_c^* \to 1$, so that it does not yield meaningful predictions. This degeneration of the model indicates that these limits are singular, which is also reflected by the fact that the bore amplitude discontinuously jumps from a finite height to zero as $\rho_c^* \to 0$ or 1, cf. figure 5(*b*), so that the flow does not smoothly transition to the full-depth lock-release case. The discussions provided by Flynn & Linden (2006) and Khodkar *et al.* (2016) shed additional light on this issue.

Consistent with the findings of Khodkar *et al.* (2016), the front speed and thickness of the lower gravity current decrease monotonically with increasing ρ_c^*, as shown in figure 6(*c*,*d*). Beyond a certain value of the intrusion density, U_l^* becomes negative,

https://doi.org/10.1017/jfm.2018.218 Published online by Cambridge University Press

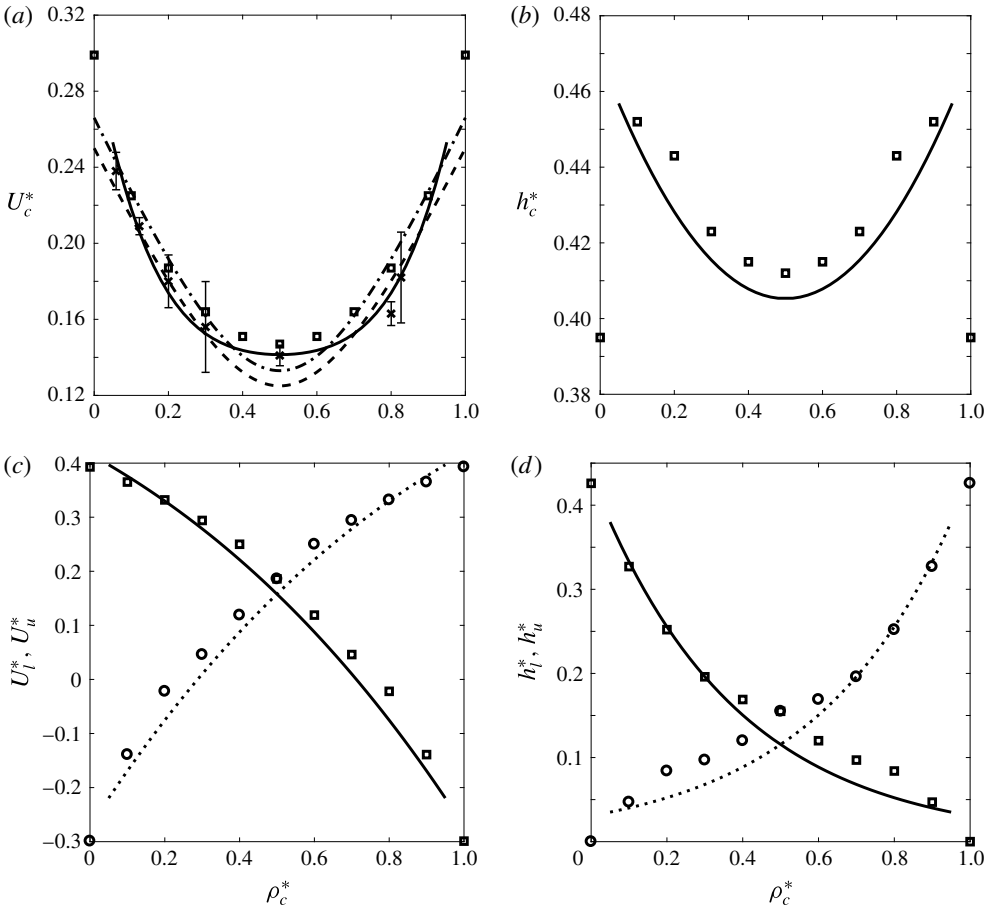


FIGURE 6. Dependence of various flow properties on the dimensionless intrusion density ρ_c^*: (*a*) intrusion front velocity U_c^*, (*b*) intrusion thickness h_c^*, (*c*) front velocities of the left-propagating gravity currents and (*d*) thicknesses of the left-propagating gravity currents. The solid lines represent the vorticity model predictions for the intrusion and lower gravity current properties, while the dotted lines denote the corresponding predictions for the upper gravity current. The dashed and dash-dotted lines indicate the results of Bolster *et al.* (2008) for the intrusion speed, when $F = 0.25$ and 0.266, respectively. The discrete circles and squares reflect the present DNS results, while the discrete crosses represent the experimental data of Bolster *et al.* (2008).

so that the front of the lower current travels towards the right. Vorticity model predictions and DNS results are seen to be in close agreement.

5. Conclusions

We have developed a vorticity-based modelling approach for intrusive gravity currents advancing into linearly stratified ambients, based on the earlier investigations of Borden & Meiburg (2013*a*), Borden & Meiburg (2013*b*) and Nasr-Azadani & Meiburg (2016). This model is the first to accurately capture the propagation velocity of the fastest-propagating internal gravity wave mode. It yields predictions for the thickness and propagation velocity of the intrusion, as functions of the intrusion

https://doi.org/10.1017/jfm.2018.218 Published online by Cambridge University Press

density, which are in close agreement with direct numerical simulations and earlier experimental and computational observations by other investigators. It is also the first model to predict the properties of the top-/bottom-propagating gravity currents. The model confirms the formation of equilibrium intrusions when the density of the intrusion fluid equals the mean density of the ambient fluid, and non-equilibrium intrusions otherwise. Consistent with previously reported observations (Bolster *et al.* 2008; Munroe *et al.* 2009; Maurer & Linden 2014), the model predicts the minimum propagation velocity to occur for equilibrium intrusions.

Acknowledgements

The authors gratefully acknowledge support through NSF Grant No. CBET-1335148.

REFERENCES

Bolster, D. T., Hang, A. & Linden, P. F. 2008 The front speed of intrusions into a continuously stratified medium. *J. Fluid Mech.* **594**, 369–377.

Borden, Z. & Meiburg, E. 2013*a* Circulation-based models for boussinesq gravity currents. *Phys. Fluids* **25** (10), 101301.

Borden, Z. & Meiburg, E. 2013*b* Circulation-based models for boussinesq internal bores. *J. Fluid Mech.* **726**, R1.

Cheong, H.-B., Kuenen, J. J. P. & Linden, P. F. 2006 The front speed of intrusive gravity currents. *J. Fluid Mech.* **552**, 1–11.

Flynn, M. R. & Linden, P. F. 2006 Intrusive gravity currents. *J. Fluid Mech.* **568**, 193–202.

Holyer, J. Y. & Huppert, H. E. 1980 Gravity currents entering a two-layer fluid. *J. Fluid Mech.* **100**, 739–767.

Khodkar, M. A., Nasr-Azadani, M. M. & Meiburg, E. 2016 Intrusive gravity currents propagating into two-layer stratified ambients: vorticity modeling. *Phys. Rev. Fluids* **1** (4), 044302.

Long, R. R. 1953 Some aspects of the flow of stratified fluids. I. A theoretical investigation. *Tellus* **5**, 42–58.

Lowe, R. J., Linden, P. F. & Rottman, J. W. 2002 A laboratory study of the velocity structure in an intrusive gravity current. *J. Fluid Mech.* **456**, 33–48.

Maurer, B. D., Bolster, D. T. & Linden, P. F. 2010 Intrusive gravity currents between two stably stratified fluids. *J. Fluid Mech.* **647**, 53–69.

Maurer, B. D. & Linden, P. F. 2014 Intrusion-generated waves in a linearly stratified fluid. *J. Fluid Mech.* **752**, 282–295.

Maxworthy, T., Leilich, J., Simpson, J. E. & Meiburg, E. H. 2002 The propagation of a gravity current into a linearly stratified fluid. *J. Fluid Mech.* **453**, 371–394.

McEwan, A. D. & Baines, P. G. 1974 Shear fronts and an experimental stratifed shear flow. *J. Fluid Mech.* **63**, 257–272.

Munroe, J. R., Voegeli, C., Birman, V., Sutherland, B. R. & Meiburg, E. H. 2009 The front speed of intrusions into a continuously stratified medium. *J. Fluid Mech.* **635**, 245–273.

Nasr-Azadani, M. M., Hall, B. & Meiburg, E. 2013 Polydisperse turbidity currents propagating over complex topography: comparison of experimental and depth-resolved simulation results. *Comput. Geosci.* **53**, 141–153.

Nasr-Azadani, M. M. & Meiburg, E. 2011 TURBINS: an immersed boundary, Navier–Stokes code for simulation of gravity and turbidity currents interacting with complex topographies. *J. Comput. Fluids* **45** (1), 14–28.

Nasr-Azadani, M. M. & Meiburg, E. 2016 Gravity currents propagating into ambients with arbitrary shear and density stratification: vorticity-based modelling. *Q. J. R. Meteorol. Soc.* **778**, 1359–1370.

https://doi.org/10.1017/jfm.2018.218 Published online by Cambridge University Press

DE ROOIJ, F., LINDEN, P. F. & DALZIEL, S. B. 1999 Saline and particle-driven interfacial intrusions. *J. Fluid Mech.* **389**, 303–334.

SUTHERLAND, B. R., KYBA, P. J. & FLYNN, M. R. 2004 The front speed of intrusive gravity currents. *J. Fluid Mech.* **514**, 327–353.

UNGARISH, M. 2005 Intrusive gravity currents in a stratified ambient: shallow-water theory and numerical results. *J. Fluid Mech.* **535**, 287–323.

UNGARISH, M. 2006 On gravity currents in a linearly stratified ambient: a generalization of Benjamin's steady-state propagation results. *J. Fluid Mech.* **548**, 49–68.

UNGARISH, M. 2009 *An Introduction to Gravity Currents and Intrusions*. Chapman & Hall/CRC Press.

UNGARISH, M. & HUPPERT, H. E. 2002 On gravity currents propagating at the base of a stratified ambient. *J. Fluid Mech.* **458**, 283–301.

UNGARISH, M. & HUPPERT, H. E. 2006 Energy balances for propagating gravity currents: homogeneous and stratified ambients. *J. Fluid Mech.* **565**, 363–380.

WHITE, B. L. & HELFRICH, K. R. 2008 Gravity currents and internal waves in a stratified fluid. *J. Fluid Mech.* **616**, 327–356.

https://doi.org/10.1017/jfm.2018.218 Published online by Cambridge University Press